Temperature-Dependent Chiral-Induced Spin Selectivity Effect: Experiments and Theory

Tapan Kumar Das, Francesco Tassinari, Ron Naaman,* and Jonas Fransson*

Cite This: *J. Phys. Chem. C* 2022, 126, 3257–3264

Read Online

ACCESS | Metrics & More | Article Recommendations | Supporting Information

ABSTRACT: The theoretical explanation for the chiral-induced spin selectivity effect, in which electrons' passage through a chiral system depends on their spin and the handedness of the system, remains incomplete. Although most experimental work was performed at room temperature, most of the proposed theories did not include vibrations. Here, we present temperature-dependent experiments and a theoretical model that captures all observations and provides spin polarization values that are consistent with the experimental results. The model includes the vibrational contribution to the spin orbit coupling. It highlights the importance of dissipation and the relation between the effect and the optical activity. The model explains the main features related to the chiral-induced spin selectivity effect and provides a new framework for future calculations and experiments.
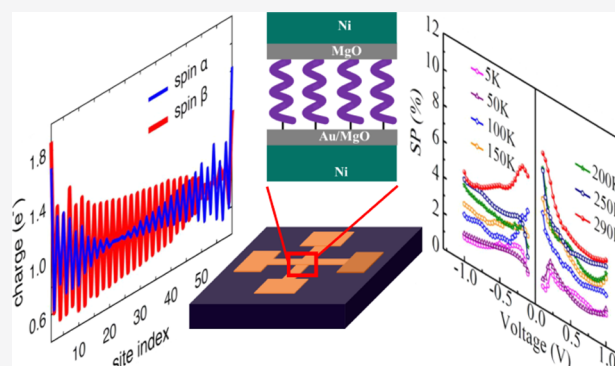
1. INTRODUCTION

In common spintronics devices, the spin polarized current usually requires a ferromagnetic electrode; their performance typically improves with decreasing temperature. In the case of the chiral-induced spin selectivity (CISS) effect,[1] these aspects seem to be different. When electrons move through a chiral electrostatic potential, one spin is preferred for electrons in motion; that is, the chiral potential tends to sort electrons with a specific spin. Hence, it is possible to obtain spin-dependent currents using chiral materials without the need for ferromagnets. Since chiral molecules are important building blocks of all organisms, the question is whether the CISS effect is efficient at the relevant temperatures for any life form. The temperature dependence of CISS should also provide an insight into the mechanism underlying the effect. There have been many attempts to theoretically explain the CISS effect.[2−27] They resulted in providing some indication of the underlying mechanism and show that the helical form of the electrostatic potential is responsible for spin-selective transport. Quantitatively, however, most calculations have failed to retain the magnitude of spin selectively observed experimentally. The failure of the models was associated with the small spin orbit coupling (SOC) typically relevant for hydrocarbons and for the carbon atom itself.[14,28] It was suggested that one has to either replace the spin selectivity with angular momentum selectivity and associate the spin observed with the SOC in the leads[29−31] or that there are other enhancement mechanisms that magnify the effect of the small SOC.[5,13,17,32]

Although most of the CISS-related experiments were performed at room temperature,[1] the model calculations usually do not include any temperature effects. In the meantime, it also became apparent that zero kelvin single channel models are not consistent with the experimental observations and that a discrepancy exists between the symmetry arguments raised, based on these models, and the observations.[33,34] Despite that these models indicate that two-point contact experiments are unable to measure the spin-polarization in the linear regime, various experiments showed that they did.[35]

Recently, several model calculations have resulted in large spin polarization (SP) when polaron[21] or vibrational effects[20,22] were considered. Moreover, accumulating evidence indicates that the CISS mechanism must include some additional features, since a correlation was found between the extent of SP, when conducting through chiral molecules, and their optical activity.[36−38] In other words, there has to be a coupling between the electronic states and some other degrees of freedom for the effect to occur.

The temperature dependence of the CISS effect may provide essential insights into the mechanism. This is indeed the focus of the present work that shows a clear enhancement of the effect with increasing temperature and a very good quantitative fit between the experiments and a model that includes the vibrational effect.
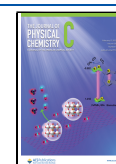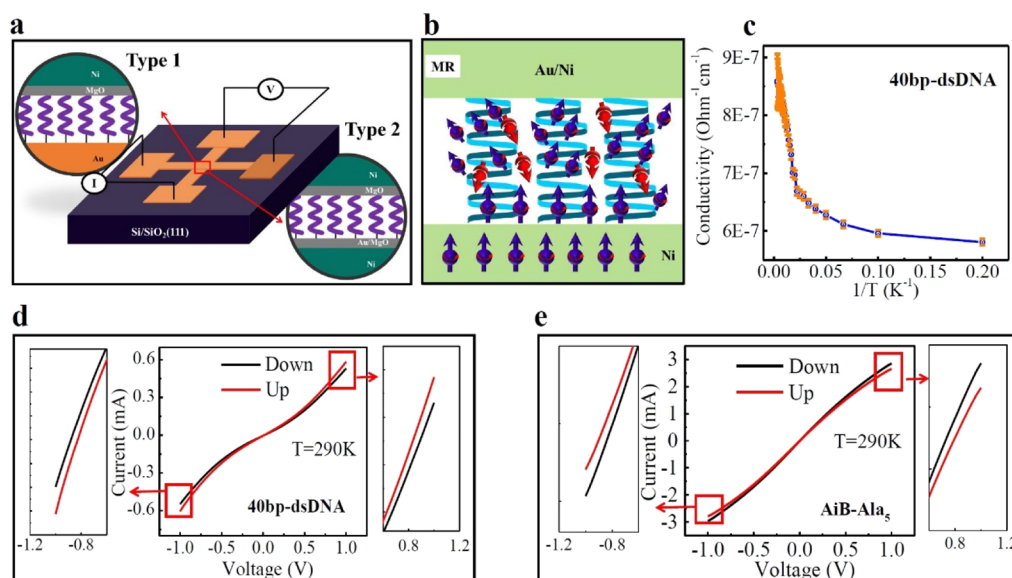
Figure 1. Experimental setup and current vs the voltage measurements. (a) Schematic of a four-probe MR presenting the two types of devices. In type 1, only one electrode is ferromagnetic, whereas in type 2, the two electrodes are ferromagnetic. (b) Typical trajectories of the electrons inside the device. Because of the large dimensions of the electrodes relative to the molecular size, electrons are collected from a wide angle, namely, also from scattered electrons whose spin direction was randomized within the monolayer. Hence, the net SP is reduced. (c) Conductivity vs $1/T$ for the 40 bp-dsDNA. The error bars are shown in orange. (d,e) Current vs the voltage ($I-V$) curves for devices recorded at 290 K for (d) 40 bp-long dsDNA and (e) [AiB-Ala]$_5$, when the current and magnetic fields are in the same direction for magnet up (red) and in the opposite directions for magnet down (black).

2. METHODS

2.1. Magnetoresistance Device Fabrication and Measurement.
The magnetoresistance (MR) measurements were performed in a crossbar geometry on a SiO$_2$ wafer. For the type 1 design, the bottom electrode had a 2 μm width; it consisted of 8 nm titanium (Ti) as an adhesive layer and 40 nm gold (Au), respectively, prepared by optical lithography. This bottom electrode is used to grow a self-assembled monolayer (SAM) of a given molecule. Prior to using MgO as the buffer layer, SAM on the device was immersed in 1 mM of 1-hexadecanethiol overnight to fill the pin hole with SAM. On top of the closely packed monolayer of the molecules, insulating buffer layers of 1.5 nm magnesium oxide (MgO) were grown by e-beam evaporation and then the final top electrode, composed of Ni and Au, and having a thickness of 40 and 20 nm, respectively, was evaporated using a shadow mask with a line width of 50 μm. Two types of (type 2) devices having two ferromagnetic electrodes were fabricated for the MR studies. Design 1 is for oligo peptides and design 2 is for ds-DNA-based devices.

2.1.1. Design 1. Design 1 of type 2 for Oligopeptides: the bottom electrode, having a 2 μm width, consisted of 8 nm titanium (Ti) as the adhesive layer and 40 nm nickel (Ni), followed by 1.5 to 2 nm MgO. The SAM of oligopeptides was grown on top of the MgO surface for 24 h.

2.1.2. Design 2. Design 2 of type 2 for ds-DNA: the bottom electrode, having a 2 μm width, consisted of 8 nm titanium (Ti) as the adhesive layer and 40 nm nickel (Ni), respectively, followed by 5 nm gold (Au) prepared by optical lithography. The SAM of ds-DNA was grown on top of the Au surface for 24 h.

On top of the closely packed monolayer of the molecules for both designs, insulating buffer layers of 1.5 to 2 nm magnesium oxide (MgO), followed by Ni and Au having a thickness of 40 and 20 nm, respectively, were evaporated using a shadow mask

with a line width of 50 μm. All electrical measurements were carried out within the cryogenics system made by Cryogenics, Ltd. A magnetic field of up to 0.9 T was applied perpendicular to the sample plane and the resistance of the device was measured using the standard four-probe method. A constant current of 0.01 mA was applied using a Keithley current source (model 2400) and the voltage across the junction was measured using a Keithley nanovoltmeter (model 2182A). The current–voltage ($I-V$) measurements were also carried out in the same device with magnet up and magnet down and with a field value of 1 T perpendicular to the device plane in four-probe electrical connections.

2.2. Surface Treatment for Monolayer Preparation.
The bottom electrodes were used for SAM. Therefore, before the SAM of the dsDNA and Ala$_5$ peptides were grown on top of the surfaces, the surfaces were cleaned in boiling acetone and boiling ethanol for 10 min each. Afterwards, they were kept in a UV ozone plasma cleaner for 15 min, which helps to remove all organic residues. Then the surfaces were incubated in normal ethanol for 30 min and finally in the molecular solution overnight.

2.3. Molecules.
2.3.1. Double-Stranded DNA (dsDNA). The 40 bs-dsDNA was used for monolayer preparation and SP studies. The dsDNA was prepared using DNA oligomers 3'-functionalized with thiol groups on one strand. The molecules were prepared by a 100 μM stock solution of DNA in deionized water. The stock solution was mixed with 0.8 M phosphate-buffered saline (PBS) (K$_2$HPO$_4$/KH$_2$PO$_4$) buffer (pH = 7.2) in a 1:1 volume ratio, thus, making a 50 μM DNA solution in 0.4 M PBS buffer. Next, the solution was mixed with an equal volume of 10 mM tris(2-carboxyethyl)phosphine hydrochloride (purchased from Sigma-Aldrich) in 0.4 M PBS buffer (pH 7.2) and left for 2 h. Then the solution was purified by filtering through a Micro Bio-Spin P-30 column (purchased from Bio Rad). The final concentrations of all dsDNA were

measured by UV−vis spectroscopy using a NanoDrop spectrometer and were found to be from 20 to 30 μM. After the SAM deposition, the samples were rinsed twice with 0.4 M PBS and twice in de-ionized water.

2.3.2. Sequence. 40 bp dsDNA:

CGC TTC GCT TCG CTT CGC TTC GCT TCG CTT CGC TTC GCT T/3ThioMC3-D/

AAG CGA AGC GAA GCG AAG CGA AGC GAA GCG AAG CGA AGC G

2.3.3. Oligopeptide. The peptide Ala$_5$ solution was prepared with the following mixture: (0.625 mg mL^{-1}, using a 1:1 mixture of pH 7.0, 10 mm sodium phosphate buffer, and trifluoroethanol). The bottom electrode in the solution for SAM was left for 36 h; afterwards, the samples were rinsed twice with de-ionized water.

2.3.4. Sequence. (Ala$_5$): SHCH$_2$CH$_2$CO-{Ala-Aib}$_5$-COOH.

3. RESULTS AND DISCUSSION

3.1. Experimental Results. MR measurements were performed as described in ref 39 and in the Supporting Information. Several types of devices were used. In one configuration only one electrode is ferromagnetic, whereas in the other, both electrodes contained a ferromagnetic Ni layer. In this second configuration one design (type 1) was applied for studying the α-helix oligopeptides, the another one, type 2, for studying ds-DNA. In type 1, the bottom electrode was composed of nickel (40 nm), coated by MgO (2 nm), whereas in type 2, the bottom electrode was composed of nickel (40 nm), followed by Au (5 nm). Following the adsorption of the molecules on the bottom electrode, the top electrode was composed of 1.5 nm of MgO, followed by nickel and Au. More details are given in the Methods section and Supporting Information.

A magnetic field of up to 0.9 T was applied perpendicular to the sample plane and the resistance of the device was measured using the standard four-probe method. Two types of monolayers of chiral molecules were investigated: one is 40 bp ds-DNA with the sequence:

CGC TTC GCT TCG CTT CGC TTC GCT TCG CTT CGC TTC GCT T/3ThioMC3-D/

AAG CGA AGC GAA GCG AAG CGA AGC GAA GCG AAG CGA AGC G.

The other is a oligopeptide, SHCH$_2$CH$_2$CO-[Ala-AiB]$_5$-COOH, when Ala refers to alanine and AiB refers to 2-aminoisobutyric acid.

Figure 1a presents a scheme of the devices used. Figure 1b shows typical trajectories of the electrons inside the device. Because of the large dimension of the electrodes relative to the molecular size, the electrons were collected from a wide angle after some of them were scattered within the device. Hence, their SP is reduced compared with that measured using a magnetic contact atomic force microscope (mcAFM).[40] The temperature-dependent conduction is shown in Figure 1c. It is what one expects with the material behaving as a semiconductor.

The current versus voltage curves for the case in which the electrodes are magnetized either UP or DOWN are shown in Figure 1d,e for temperature 290 K and the temperature dependent current versus voltage curve are shown in Figure S1a,b respectively for both molecules. Very similar results were obtained for devices with a single ferromagnetic electrode (see the Supporting Information). In the DNA device, the current is

higher when the magnet points UP, whereas for the oligopeptides it is higher when the magnet points DOWN. This finding is in agreement with previous studies and is correlated with the different sign of the optical activity of the molecules.[38] More details on the functioning of the MR devices are given in the Methods section and the Supporting Information.

The temperature and voltage dependences of the SP are shown in Figures 2 and S2. Figure 2a,b show the SP as a
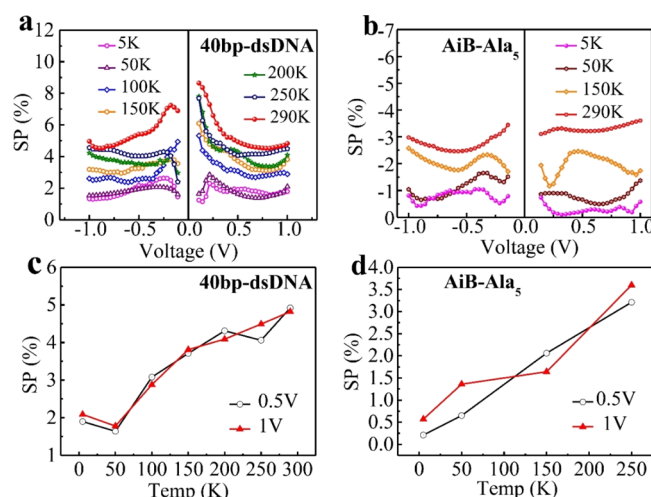

Figure 2. SP calculated from the current−voltage ($I-V$) characteristics plot for magnet-up and magnet-down. (a) SP (in %) for the 40 bp-length of dsDNA and (b) [AiB-Al]$_5$ oligopeptide measured at different temperatures. (c,d) SP as a function of temperature. SP = $(I_{up} - I_{down})/(I_{up} + I_{down}) \times 100$, where I_{up} and I_{down} are the current with spin aligned parallel and antiparallel to the magnetic field directions, respectively. The curves are given for the applied voltage 0.5 and 1 V.

function of voltage for different temperature and Figure 2c, d show the SP as a function of temperature for two specific voltage for the two molecules. The SP increases with temperature and the increase does not significantly depend on the voltage applied between the two electrodes. The calculated SP as a function of temperature and applied voltage are shown in Figure S2a,b for oligopeptide and S2c,d for ds-DNA respectively.

The MR, is defined as $=\frac{R(B) - R(0)}{R(0)}$, where $R(B)$ and $R(0)$ are the resistances measured at a magnetic field B and with no magnetic field, respectively. The MR signal, for devices containing two ferromagnetic electrodes, is shown in Figure 3. The MR curve is asymmetric (Figure 3a,b), not like the common MR that shows the same values for magnetic fields of opposite signs. The same observations were obtained for the device containing single ferromagnetic electrode (Figure S3a,b). The asymmetry was observed before for CISS.[39] The magnitude of the MR increases almost linearly with temperature (Figure 3c,d) and this is also true for the single ferromagnetic electrode based devices (Figure S4a,b). Figure S5a−c show the MR signal for three different length (30, 40 and 50 bp) of dsDNA molecules in devices containing one ferromagnetic electrode.

The experimental results indicate that the SP increases with increasing temperature. It also shows that in the current versus voltage studies (Figure 1d,e), the high current is obtained
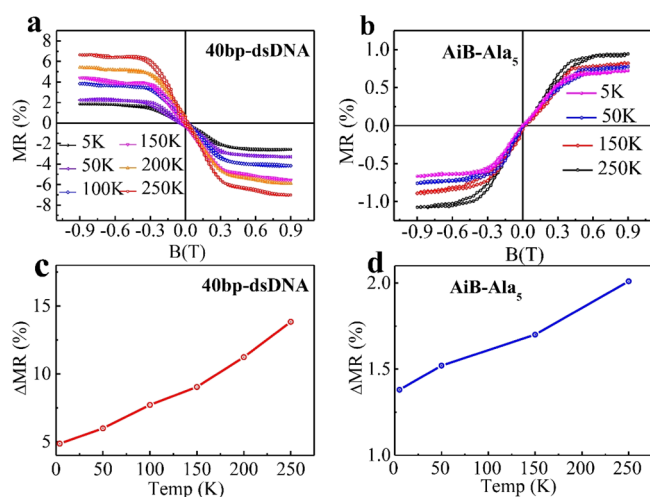
Figure 3. Temperature-dependent MR obtained with devices having two ferromagnetic electrodes. (a) A 40 bp-length of dsDNA and (b) an [AiB-Ala]$_5$ oligopeptide measured at a different temperature with an input current of 0.01 mA. (c) ΔMR (%) values as a function of temperature for 40 bp dsDNA and (d) for AiB-Al$_5$, where ΔMR (%) = MR(%)$_{0.9T}$ + MR(%)$_{-0.9T}$. Panels (c,d) indicate almost linear dependence of the change in MR on the temperature.

when the magnet is pointing in the same direction, for the two current directions. This is contrary to the observations in the common giant MR (GMR) studies. In addition, in the CISS experiments, an unexplained correlation was found between the SP and the optical activity.[36−38] Next, we present a model that explains all the phenomena observed.

3.2. Model. In many CISS-related publications, it is stated that the mechanism underlying the CISS effect is not yet understood. This statement is based on several experimental observations that seem to be inconsistent with conventional theories that focus on the ground-state properties of spintronic devices at zero temperature. The inconsistencies can be summarized as follows:

1. The SOC expected in hydrocarbons is too small to observe the large SP seen experimentally.
2. It is not expected to be able to measure SP of current having two contacts setups; however, in CISS-related experiments this was done and large SP was measured.
3. When measuring the current in the presence of a magnetic field and ferromagnetic electrodes, the conventional GMR devices exhibit an asymmetry. Namely, current flowing in one direction is stronger with the magnetic field pointing in a specific direction, whereas upon reversing the current direction the strongest current is observed with the opposite magnetic field. However, this is not the case in the CISS-related devices, where the same direction of the magnetic field gives the highest current for current going either forward or backwards. The opposite magnetic field will be associated with higher current only for molecules with opposite handedness.
4. In addition to all of the above, it seems strange that very high SP is observed in the CISS-related experiments, since it is known that the SP of the ferromagnetic electrode (Ni in our case) is only about 20%.

Next, we will present a mechanism for enhanced SOC, which is based on vibrational coupling. Based on this

mechanism, all the anomalies of the CISS effect, described above, can be explained. First, we follow refs 17 and 41, and consider the role of vibrations in the CISS effect.

We begin with the single electron Hamiltonian

$$H = \frac{p^2}{2m_e} + V(r) + \xi(\nabla V(r) \times p) \cdot \frac{\hbar}{2} \sigma \tag{1}$$

where m_e is the electron mass, $V(r)$ is the effective confinement potential, and the last term defines the SOC contribution, $L \cdot S$, in terms of the orbital and the spin degrees of freedom $L = \xi \nabla V \times p$ and $S = \hbar \sigma/2$, respectively, with $\xi = (2m_e c)^{-2}$. The operator p acts on everything to its right, whereas ∇ acts only on the component directly adjacent to its right, such that $\nabla V \times p = (\nabla V) \times p$. Finally, σ denotes the vector of Pauli matrices. Here the confinement potential $V(r)$ is developed in the vibrational coordinates $Q = r - r_0$, where r_0 denotes the equilibrium position, such that $V(r) = V(r_0) + Q \cdot \nabla V(r)|_{r \to r0} + ...$ The orbital component of the SOC, $L = \xi \nabla V \times p$, can therefore, be written as $L(r) = L_0 + \delta L(Q(r), r)$, where

$$L_0 = \xi \lim_{r \to r_0} \nabla V(r) \times p \tag{2A}$$

$$\delta L(Q(r), r) = \xi \lim_{r \to r_0} \nabla (Q \cdot \nabla V(r) + ...) \times p \tag{2B}$$

The static SOC, $L_0 \cdot S$, is the form of the SOC that is normally considered in theoretical descriptions of the CISS effect. Clearly, there is no strong temperature dependence emerging from this contribution, since it only captures the purely electronic part of this mechanism. In contrast, the correction to the static SOC, $\delta L \cdot S$, represents a vibrationally assisted correction to the SOC, which provides a direct temperature dependence, arising from the coupling between the electrons and the nuclear vibrations. This can be understood by considering that the vibrational coordinate Q constitutes the nuclear displacement, which is thermally activated and becomes finite by anharmonicity.[42]

A temperature dependence results from coherent molecular vibrations; therefore, we express the displacement operator Q in the second quantization as $Q = \sum_\mu l_\mu \epsilon_\mu (a_\mu + a_\mu^\dagger)$, where $l_\mu = \sqrt{\hbar/2\rho v \omega_\mu}$ defines a length scale in terms of the density of vibrations ρ, the system volume v, the vibrational frequency ω_μ, and the polarization vector ϵ_μ, whereas $a_\mu + a_\mu^\dagger$ represents the displacement quantum at r in the mode μ.

The quantum operators a_μ and $a_\mu^\dagger$ annihilate and create, respectively, a coherent molecular vibration mode μ. Consequently, the polarization vector ϵ_μ carries the chiral symmetry of the molecule and, therefore, enables a coupling between the angular momentum of the vibrations and the electron spin.

In the second quantization, the model introduced through eqs 1, 2A, and 2B, assumes the form

$$\mathcal{H} = \sum_m \psi_m^\dagger E_m \psi_m + \sum_\mu \omega_\mu a_\mu^\dagger a_\mu$$
$$+ \sum_{mm'\mu} \psi_m^\dagger U_{mm'\mu} \psi_{m'} (a_\mu + a_\mu^\dagger) \tag{3}$$

where $E_m = \int \phi_m^* (p^2/2m_e + V(r_0) + L_0 \cdot S) \phi_m \, dr/v$ defines the single-electron energy matrix, including the static SOC, in terms of the eigenstates $\phi_m = \phi_m(r)$, and ψ_m is the electron spinor, whereas the couplings between electrons and vibrations are defined through $U_{mm'\mu} = U_{mm'\mu} + J_{mm'\mu} \cdot \sigma$, where

$$U_{mm'\mu} = l_\mu \int \phi_m^* \epsilon_\mu \cdot \nabla V(r - r_0) \phi_{m'} \frac{dr}{v} \tag{4a}$$

$$J_{mm'\mu} = \frac{l_\mu \xi \hbar}{2} \int \phi_m^* \{\nabla[\epsilon_\mu \cdot \nabla V(\boldsymbol{r} - \boldsymbol{r}_0)] \times \boldsymbol{p}\} \phi_{m'} \frac{dr}{v} \tag{4b}$$

Here, $U_{mm'\mu}$ defines the coupling between the electronic charge and the molecular vibrations, whereas $J_{mm'\mu}$ denotes the strength of the vibrationally assisted correction to the SOC.

The roles played by $U_{mm'\mu}$ and $J_{mm'\mu}$ become clear by employing the canonical transformation $\widetilde{\mathcal{H}} = e^S \mathcal{H} e^{-S}$, where the generating operator $S = -\sum_{mm'\mu} \psi_m^\dagger U_{mm'\mu} \psi_{m'} (a_\mu - a_\mu^\dagger)/\omega_\mu$. For simplicity, we retain only a single vibrational mode, ω_0. In the limit $\boldsymbol{J} \cdot \boldsymbol{\sigma} \to J \sigma^z$, the transformation enables the exact decoupling between the Fermionic and the Bosonic degrees of freedom,[15] such that

$$\widetilde{\mathcal{H}} = \sum_m \widetilde{\mathcal{H}}_m + \sum_{m \neq m'} \widetilde{\mathcal{H}}_{mm'} + \omega_0 a_0^\dagger a_0$$

where $(U_m = U_{mm0}, J_m = J_{mm0})$

$$\widetilde{\mathcal{H}}_m = \left(E_m - \frac{U_m^2 - J_m^2}{\omega_0}\right) n_m - 4\frac{U_m J_m}{\omega_0} s_m^z$$
$$- 2\frac{U_m^2 - J_m^2}{\omega_0} n_{m\uparrow} n_{m\downarrow} \tag{5a}$$

$$\widetilde{\mathcal{H}}_{mm'} = -\frac{2}{\omega_0}(U_m U_{m'} n_m n_{m'} - 4 U_m J_{m'} n_m s_{m'}^z - 4 J_m J_{m'} s_m^z s_{m'}^z) \tag{5b}$$

given in terms of $n_{m\sigma} = \psi_m^\dagger (\sigma_0 + \sigma_{\sigma\sigma}^z \sigma^z) \psi_m/2$, $n_m = \sum_\sigma n_{m\sigma}$, and $s_m^z = \psi_m^\dagger \sigma^z \psi_m/2$.

Based on the expressions in eqs 5a and 5b, the couplings U_m and J_m can be interpreted to define vibrationally assisted electron−electron and exchange interactions, respectively. Both contributions are viable mechanisms for enhancing the magnetic response in structures with broken spin symmetry. However, the magnetic response for purely electron−electron interactions is largely defined by the asymmetry between the spin densities, whereas the energy difference between the spin states may be negligible. Such asymmetry is expected to be significant for transport only at low temperatures. In contrast, the effective exchange interaction may induce a splitting between the energies of the electronic spin states. This mechanism is therefore expected to dominate the response at higher temperatures. The combination of the two vibrationally assisted couplings generates a strong CISS effect, which was reported in ref 17.

We will now address the temperature dependence of the vibrationally generated interactions by employing a tight-binding model[17,41] represented by $\mathcal{H}_{mol} = \mathcal{H}_0 + \mathcal{H}_{vib}$, (see the Supporting Information). Here, $\mathcal{H}_0$ is the static contribution to the electronic energy, comprising the electron levels, ε_m, the nearest-neighbor interaction, t_0, and static SOC through the next nearest-neighbor interaction, λ_0. Furthermore, $\mathcal{H}_{vib}$ comprises a spin-independent vibrationally assisted nearest-neighbor interaction, t_1, and a vibrationally assisted next nearest-neighbor SOC, λ_1. The parameters t_1 and λ_1 represent the interactions $U_{mm'\mu}$ and $J_{mm'\mu}$, respectively. Upon mounting the model of the chiral molecule between metallic leads, where one is ferromagnetic with a SP parametrized by $p_L \in [-1,1]$, the charge is redistributed in the molecule,

accompanied by the emergence of a finite SP.[17,41] We calculated the charge current $I_\pm$ for a given SP $p_L = \pm 0.5$ in the ferromagnetic lead, as discussed in refs 17 and 22.

The charge current is calculated using the expression

$$J = \frac{ie}{h} sp \int \Gamma^L(\sigma)(f_L(\omega) \boldsymbol{G}_1^>(\omega) + f_L(-\omega) \boldsymbol{G}_1^<(\omega)) d\omega \tag{6}$$

where e and h is the electron charge and Planck's constant, respectively, whereas $\Gamma^L(\sigma)$ defines the coupling strength between the ferromagnetic lead and the adjacent (first) site in the chiral molecule, $f_L(\omega) = f(\omega - \mu_L)$ is the Fermi−Dirac distribution function for electrons in the left lead with chemical potential μ_L, and $\boldsymbol{G}_1^{</>}(\omega)$ is the lesser/greater Green function which describe the density of occupied/unoccupied states at the site adjacent to the left lead. These densities depend on the full structure represented by the model for the molecule connected to the leads.

Figure 4 presents (a) the charge current and (b) the spin selectivity, for bias voltage $V = 0.6$ V and vibrational frequency
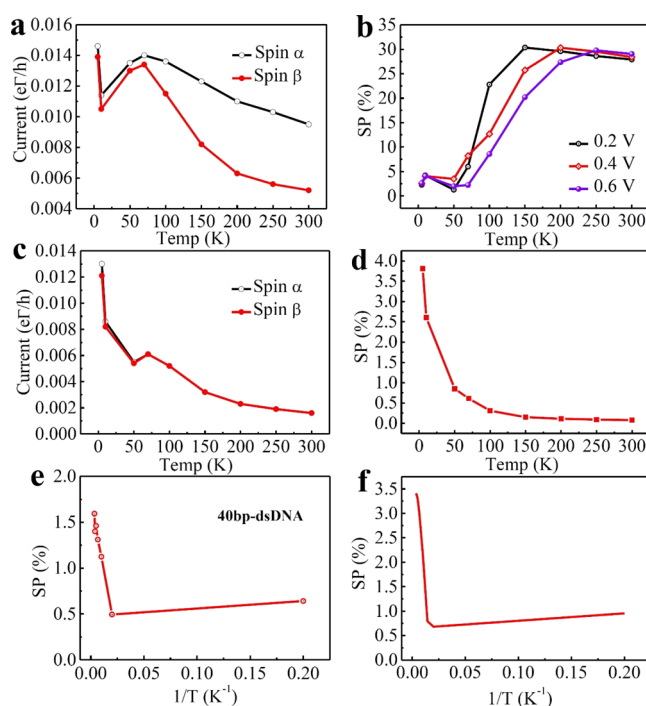

Figure 4. (a,c) Simulated charge currents under polarization conditions, $p_L = \pm 0.5$ in ferromagnetic lead, and (b,d) the corresponding spin selectivity. The parameters used are $t_0 = 40$ meV, $\lambda_0 = t_0/40$, $t_1 = t_0/10$, $\omega_0 = t_0/10,000$, $\gamma = t_0/10$, and $V = 0.6$ V. However, in (a,b) $\lambda_1 = t_0/400$ and in (c,d) $\lambda_1 = 0$, namely, in (c,d) the vibrations do not contribute to the spin part of the vibrationally enhanced SOC (eq 5b). Panels (e,f) compares the experimental results and the model calculations. (e) ln of SP(%) vs $1/T$ is shown for 40 bp-dsDNA for an applied voltage of 0.5 V. (f) Model calculations Ln of SP(%) vs $1/T$ with parameters as in (a,b).

$\omega_0 = 4$ μeV, where the latter is chosen since it gives a good fitting. One similarity in the charge currents is the overall decay with increasing temperature. However, the decay strongly depends on the sign of the SP, p_L. This results from the spin-dependent dissipation introduced by the vibrations. Charge currents for bias voltages $V = 0.2$ and 0.4 V are shown in Figure S6a,b. At low temperatures, the vibrational excitation is
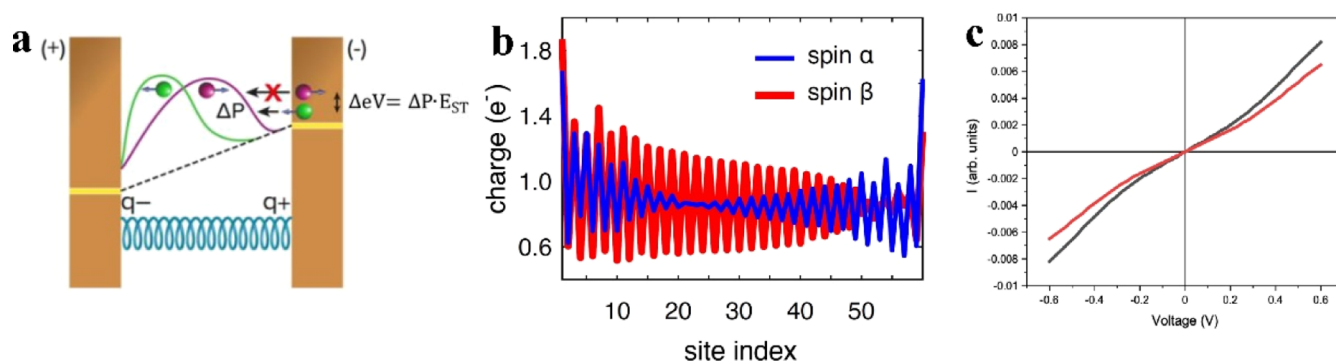
Figure 5. (a) Scheme describing the mechanism underlying the CISS effect in terms of the SP, ΔP, which arises from the SOC. This SP causes a spin blockade, ΔeV, because of the Pauli principle, which is proportional to the singlet-triplet energy gap, E_{ST}, in the molecule. The purple and green curves represent the charge distribution occurring upon applying the field across the molecule, for electrons with spin aligned parallel (green) or antiparallel (purple) to their velocities. The molecule is presented schematically as a coil. The yellow lines indicate the Fermi energy at each electrode and the dotted line shows the electric field across the molecule, assuming a molecule with a very low dielectric constant. (b) Model-based calculation for the non-equilibrium spin distribution in a chiral molecule positioned between two non-magnetic leads, at the voltage bias $V = 0.24$ V. Note that there is an excess of spin α on the right end of the molecule and of spin β on the left end. (c) Model-based calculation of the current vs voltage curves for electrons injected from a ferromagnetic electrode magnetized with the magnetic moment pointing away from the molecule (black) or toward the molecule (red). Figure 5a is copied with the permission from ref 49.

low, which leads to a small effect of the inelastic scattering. With increasing temperature, however, the vibrational excitations increase; this enhances the inelastic scattering. Therefore, the current decreases with increasing temperature.

The source of the spin-dependent dissipation is the vibrationally assisted SOC. There are three different vibrationally assisted processes to the second order in the interactions between sites:[16,41] (i) on-site and the second neighbor hopping, (ii) on-site and the fourth neighbor SOC, and (iii) the first and third neighbor mixed hopping and SOC. The first type of process is proportional to $t_1^2 \Sigma_m$, where Σ_m is the electron−phonon interaction loop at the site m; its contribution to the dissipation is spin symmetric. The second contribution is proportional to $\lambda_1^2 v_m^{(s)} \cdot \sigma v_{m+2s}^{(s')} \cdot \sigma \Sigma_m$, where the (unit) vector $v_m^{(s)}$ defines the chirality, and $s, s' = \pm 1$. The on-site processes are spin symmetric (see the Supporting Information). The fourth neighbor SOC breaks the spin symmetry, since the involved chirality vectors, $v_m^{(\pm)}$ and $v_{m\pm2}^{(\mp)}$, are not parallel. However, the effect is the second order in the SOC parameter λ_1, which necessarily is small. In contrast, the third types of processes, the first and third neighbor mixed hopping and SOC, which are proportional to $it_1\lambda_1 v_m^{(s)} \cdot \sigma \Sigma_m$ and $it_1\lambda_1 v_{m+s}^{(s')} \cdot \sigma \Sigma_m$, respectively, provide vibrationally assisted SOC to the first order in λ_1 and break the spin symmetry. The temperature dependence of Σ_m is dominated by thermally occupied vibrational excitations (Bose−Einstein distribution). Owing to the scaling factors t_1^2 and $t_1\lambda_1$, the temperature effect is shifted to higher energies than what is nominally suggested by the vibrational frequency. Hence, for $\omega_0 = 4$ μeV and the other parameters used here, a spin asymmetry between the currents would begin between 50 and 100 K, as shown in Figure 4a. The fact that the temperature dependence of the break in the spin symmetry is associated with mixed hopping and SOC processes is demonstrated in Figure 4c, where the spin currents are calculated in the absence of the vibrationally assisted SOC. With increasing temperature, the two currents become increasingly equal, as confirmed by the decreasing SP (Figure 4d). The remaining spin asymmetry is attributed to the vibrationally induced electron−electron interaction, c.f. eq 5a.

The non-monotonic behavior in both the current and the spin selectivity is a signature of competing effects. The spin

selectivity increases as long as the spin-dependent processes dominate dissipation. In contrast, when the spin symmetric processes become the dominating source for dissipation, the spin selectivity decays. The vibrationally induced electron−electron and exchange interactions scale as $1/\omega_\mu$ (see Figure S7) and both are reduced for high vibrational frequencies.

In Figure 4e the SPs are presented as an Arrhenius plot. It is clear that a barrier of about 50k exists for the increased SP. These barriers correspond to low vibrational frequencies; hence, they refer to vibrations that include a large part of the oligomer.

The model reproduces the experimental results with excellent agreement, as shown in Figure 4f. We wish to emphasize that the model did not attempt to precisely represent the system, and it does not correctly represent all the molecular features. We also notice that the nearly metallic model for the molecule that leads to a decreasing current with the temperature used here can be replaced by a semiconducting molecule for which the current increases with the temperature, without losing the obtained temperature dependence of the CISS effect. However, apparently the temperature effect is not very sensitive to those features.

The model relates the SP to the molecular polarizability, through ϵ_μ in eq 4a and 4b. It is well established that the polarizability is proportional to the optical activity.[43,44] Hence, the model relates the SP to the optical activity of the molecules. The model also indicates the importance of coupling with low-frequency vibrations/phonons, which means that the electron transmission through the molecules is not ballistic, but instead involves dissipation. It also results in the same symmetry in the $I−V$ curves, as observed in all the CISS results (see the Supporting Information, Figure S8). Therefore, the model is consistent with the observations of coupling between electron spin and the acoustic chiral phonons in inorganic crystals.[45−48]

Because the CISS effect, as described here, is not a ground state property and it involves dissipation, the argument regarding the ability to measure SP by a two-contact setup is not relevant anymore, since it is expected that for multilevel systems that include dissipation, the argument presented by Onsager[34] is invalid.

The symmetry in the current versus voltage obtained is consistent with the model presented. When an electric potential is applied on a chiral molecule, the molecule is charge polarized. Since the charge polarization is accompanied by SP, each electric pole is associated with a specific spin (see Figure 5a,b). Indeed, the charge density at each pole can be less than a full electron. Figure 5b shows the calculated non-equilibrium spin distribution in the model molecule and indicates that indeed a different spin is associated with each side of the molecule. In the case of molecules with one specific handedness, for current moving from right to left, as in Figure 5a, there is a different barrier for injecting one spin versus the other from the electrode into the molecule. The difference in the barriers, ΔeV, is proportional to the extent of SP, ΔP, at the pole near the electrode times the spin exchange interaction, E_{ST}, which is related to the singlet−triplet splitting in the molecule. Consequently, one magnetic direction of the electrode, which injects mainly one spin, generates a higher current than the other direction. For current moving from left to right, the opposite spin is preferred; hence the electrons will be injected from the minority states. However, because the molecule−electrode interface defines the probability for a certain spin current, the larger current will also be injected here in the same magnetic direction as for current moving from right to left. Hence, the same preferred magnet direction will be relevant for current flowing to the left or to the right. The current versus voltage curves were calculated based on the model and are shown in Figure 5c.

The model presented in Figure 5 also explains the SP measured, which exceeds the SP of the ferromagnet. In addition to the ferromagnet, there is a spin-dependent barrier at the interface between the electrode and the molecule; it further enhances the polarization. A mechanism that sustains the large difference between the spin-dependent barriers is provided by the nuclear vibrations that couple to the electrons.

4. CONCLUSIONS

The experimental results, the model, and the fitting between them explain why the zero temperature models fail to obtain the magnitude of the CISS effect and its qualitative behavior in terms of symmetry constraints. The vibrationally induced enhanced spin selectivity results from non-Born−Oppenheimer interactions. It is not necessarily the only mechanism for enhancing the SOC, as pointed out in other recent works that involve polarons,[21] Berry phases, and Jahn Teller effects.[13,23] However, in all those cases, it is important to understand that SP that accompanies charge polarization contributes to the relaxation of the symmetry constraints that exist in the zero temperature models. Moreover, it is important to understand that charge polarization can be induced not only by applying an electric field with electrodes, but also in the case of electron transfer systems, when a donor group is photoexcited. In such a case, a difference in electrochemical potential occurs between the donor and acceptor, which is equivalent to applying an electric field.

It is a challenge to transfer the model presented here to ab-initio calculations, since the processes are time-dependent and involve many states including non-Born Oppenheimer interactions. However, the model presents a framework to better understand the CISS effect and the parameters that affect its magnitude.

■ ASSOCIATED CONTENT

ⓢ Supporting Information

The Supporting Information is available free of charge at https://pubs.acs.org/doi/10.1021/acs.jpcc.1c10550.

Additional details on the device fabrication; surface treatment for monolayer preparation and the details of the molecules; temperature-dependent current versus voltage curve; SP versus temperature; MR of single ferromagnetic electrode device; total MR (ΔMR) spectra with temperature; length and temperature-dependent MR spectra; simulated change current with vibration; simulated charge current without vibration and SP; and current versus voltage based on the model calculations (PDF)

■ AUTHOR INFORMATION

Corresponding Authors

Ron Naaman − *Department of Chemical and Biological Physics, Weizmann Institute, Rehovot 7610001, Israel;* ⓘ orcid.org/0000-0003-1910-366X; Email: ron.naaman@weizmann.ac.il

Jonas Fransson − *Department of Physics and Astronomy, Uppsala University, Uppsala 752 36, Sweden;* ⓘ orcid.org/0000-0002-9217-2218; Email: jonas.fransson@physics.uu.se

Authors

Tapan Kumar Das − *Department of Chemical and Biological Physics, Weizmann Institute, Rehovot 7610001, Israel;* ⓘ orcid.org/0000-0001-7918-5973

Francesco Tassinari − *Department of Chemical and Biological Physics, Weizmann Institute, Rehovot 7610001, Israel*

Complete contact information is available at:
https://pubs.acs.org/10.1021/acs.jpcc.1c10550

Notes

The authors declare no competing financial interest.

■ ACKNOWLEDGMENTS

■ REFERENCES

(1) Waldeck, D. H.; Naaman, R.; Paltiel, Y. The spin selectivity effect in chiral materials. *APL Mater.* **2021**, *9*, 040902.

(2) Díaz, E.; Contreras, A.; Hernández, J.; Domínguez-Adame, F. Effective nonlinear model for electron transport in deformable helical molecules. *Phys. Rev. E* **2018**, *98*, 052221.

(3) Yang, X.; van der Wal, C. H.; van Wees, B. J. Spin-dependent electron transmission model for chiral molecules in mesoscopic devices. *Phys. Rev. B* **2019**, *99*, 024418.

(4) Díaz, E.; Albares, P.; Estévez, P. G.; Cerveró, J. M.; Gaul, C.; Diez, E.; Domínguez-Adame, F. Spin dynamics in helical molecules with nonlinear interactions. *New J. Phys.* **2018**, *20*, 043055.

(5) Michaeli, K.; Naaman, R. Origin of Spin-Dependent Tunneling Through Chiral Molecules. *J. Phys. Chem. C* **2019**, *123*, 17043−17048.

(6) Gutierrez, R.; Díaz, E.; Naaman, R.; Cuniberti, G. Spin-selective transport through helical molecular systems. *Phys. Rev. B: Condens. Matter Mater. Phys.* **2012**, *85*, 081404.

(7) Guo, A.-M.; Sun, Q.-f. Spin-Selective Transport of Electrons in DNA Double Helix. *Phys. Rev. Lett.* **2012**, *108*, 218102.

(8) Guo, A.-M.; Sun, Q.-F. Spin-dependent electron transport in protein-like single-helical molecules. *Proc. Natl. Acad. Sci. U.S.A.* **2014**, *111*, 11658−11662.

(9) Rai, D.; Galperin, M. Electrically Driven Spin Currents in DNA. *J. Phys. Chem. C* **2013**, *117*, 13730−13737.

(10) Matityahu, S.; Utsumi, Y.; Aharony, A.; Entin-Wohlman, O.; Balseiro, C. A. Spin-dependent transport through a chiral molecule in the presence of spin-orbit interaction and nonunitary effects. *Phys. Rev. B* **2016**, *93*, 075407.

(11) Varela, S.; Mujica, V.; Medina, E. Effective spin-orbit couplings in an analytical tight-binding model of DNA: Spin filtering and chiral spin transport. *Phys. Rev. B* **2016**, *93*, 155436.

(12) Behnia, S.; Fathizadeh, S.; Akhshani, A. Modeling spin selectivity in charge transfer across the DNA/Gold interface. *Chem. Phys.* **2016**, *477*, 61−73.

(13) Dalum, S.; Hedegård, P. Theory of Chiral Induced Spin Selectivity. *Nano Lett.* **2019**, *19*, 5253−5259.

(14) Maslyuk, V. V.; Gutierrez, R.; Dianat, A.; Mujica, V.; Cuniberti, G. Enhanced Magnetoresistance in Chiral Molecular Junctions. *J. Phys. Chem. Lett.* **2018**, *9*, 5453−5459.

(15) Díaz, E.; Domínguez-Adame, F.; Gutierrez, R.; Cuniberti, G.; Mujica, V. Thermal Decoherence and Disorder Effects on Chiral-Induced Spin Selectivity. *J. Phys. Chem. Lett.* **2018**, *9*, 5753−5758.

(16) Zöllner, M. S.; Varela, S.; Medina, E.; Mujica, V.; Herrmann, C. Insight into the Origin of Chiral-Induced Spin Selectivity from a Symmetry Analysis of Electronic Transmission. *J. Chem. Theory Comput.* **2020**, *16*, 2914−2929.

(17) Fransson, J. Chirality-Induced Spin Selectivity: The Role of Electron Correlations. *J. Phys. Chem. Lett.* **2019**, *10*, 7126−7132.

(18) Ghazaryan, A.; Lemeshko, M.; Volosniev, A. G. Filtering spins by scattering from a lattice of point magnets. *Commun. Phys.* **2020**, *3*, 178.

(19) Shitade, A.; Minamitani, E. Geometric spin-orbit coupling and chirality-induced spin selectivity. *New J. Phys.* **2020**, *22*, 113023.

(20) Du, G.-F.; Fu, H.-H.; Wu, R. Vibration-enhanced spin-selective transport of electrons in the DNA double helix. *Phys. Rev. B* **2020**, *102*, 035431.

(21) Zhang, L.; Hao, Y.; Qin, W.; Xie, S.; Qu, F. Chiral-induced spin selectivity: A polaron transport model. *Phys. Rev. B* **2020**, *102*, 214303.

(22) Fransson, J. Vibrational origin of exchange splitting and ″chiral-induced spin selectivity. *Phys. Rev. B* **2020**, *102*, 235416.

(23) Bian, X.; Wu, Y.; Teh, H.-H.; Zhou, Z.; Chen, H.-T.; Subotnik, J. E. Modeling nonadiabatic dynamics with degenerate electronic states, intersystem crossing, and spin separation: A key goal for chemical physics. *J. Chem. Phys.* **2021**, *154*, 110901.

(24) Alwan, S.; Dubi, Y. Spinterface Origin for the Chirality-Induced Spin-Selectivity Effect. *J. Am. Chem. Soc.* **2021**, *143*, 14235−14241.

(25) Fay, T. P.; Limmer, D. T. Origin of Chirality Induced Spin Selectivity in Photoinduced Electron Transfer. *Nano Lett.* **2021**, *21*, 6696−6702.

(26) Hoff, D. A.; Rego, L. G. C. Chirality-Induced Propagation Velocity Asymmetry. *Nano Lett.* **2021**, *21*, 8190−8196.

(27) Volosniev, A. G.; Alpern, H.; Paltiel, Y.; Millo, O.; Lemeshko, M.; Ghazaryan, A. Interplay between friction and spin-orbit coupling as a source of spin polarization. *Phys. Rev. B* **2021**, *104*, 024430.

(28) Yeganeh, S.; Ratner, M. A.; Medina, E.; Mujica, V. Chiral electron transport: Scattering through helical potentials. *J. Chem. Phys.* **2009**, *131*, 014707.

(29) Skourtis, S. S.; Beratan, D. N.; Naaman, R.; Nitzan, A.; Waldeck, D. H. Chiral Control of Electron Transmission through Molecules. *Phys. Rev. Lett.* **2008**, *101*, 238103.

(30) Gersten, J.; Kaasbjerg, K.; Nitzan, A. Induced spin filtering in electron transmission through chiral molecular layers adsorbed on metals with strong spin-orbit coupling. *J. Chem. Phys.* **2013**, *139*, 114111.

(31) Liu, Y.; Xiao, J.; Koo, J.; Yan, B. Chirality-driven topological electronic structure of DNA-like materials. *Nat. Mater.* **2021**, *20*, 638−644.

(32) Wu, Y.; Subotnik, J. E. Electronic spin separation induced by nuclear motion near conical intersections. *Nat. Commun.* **2021**, *12*, 700.

(33) Rikken, G. L. J. A.; Fölling, J.; Wyder, P. Electrical Magnetochiral Anisotropy. *Phys. Rev. Lett.* **2001**, *87*, 236602.

(34) Yang, X.; van der Wal, C. H.; van Wees, B. J. Detecting Chirality in Two-Terminal Electronic Nanodevices. *Nano Lett.* **2020**, *20*, 6148−6154.

(35) Liu, T.; Wang, X.; Wang, H.; Shi, G.; Gao, F.; Feng, H.; Deng, H.; Hu, L.; Lochner, E.; Schlottmann, P.; et al. Linear and Nonlinear Two-Terminal Spin-Valve Effect from Chirality-Induced Spin Selectivity. *ACS Nano* **2020**, *14*, 15983−15991.

(36) Bloom, B. P.; Graff, B. M.; Ghosh, S.; Beratan, D. N.; Waldeck, D. H. Chirality Control of Electron Transfer in Quantum Dot Assemblies. *J. Am. Chem. Soc.* **2017**, *139*, 9038−9043.

(37) Kulkarni, C.; Mondal, A. K.; Das, T. K.; Grinbom, G.; Tassinari, F.; Mabesoone, M. F. J.; Meijer, E. W.; Naaman, R. Highly Efficient and Tunable Filtering of Electrons' Spin by Supramolecular Chirality of Nanofiber-Based Materials. *Adv. Mater.* **2020**, *32*, 1904965.

(38) Mondal, A. K.; Preuss, M. D.; Śleczkowski, M. L.; Das, T. K.; Vantomme, G.; Meijer, E. W.; Naaman, R. Spin Filtering in Supramolecular Polymers Assembled from Achiral Monomers Mediated by Chiral Solvents. *J. Am. Chem. Soc.* **2021**, *143*, 7189−7195.

(39) Mathew, S. P.; Mondal, P. C.; Moshe, H.; Mastai, Y.; Naaman, R. Non-magnetic organic/inorganic spin injector at room temperature. *App. Phys. Lett.* **2014**, *105*, 242408.

(40) Mishra, S.; Mondal, A. K.; Pal, S.; Das, T. K.; Smolinsky, E. Z. B.; Siligardi, G.; Naaman, R. Length-Dependent Electron Spin Polarization in Oligopeptides and DNA. *J. Phys. Chem. C* **2020**, *124*, 10776−10782.

(41) Fransson, J. Charge Redistribution and Spin Polarization Driven by Correlation Induced Electron Exchange in Chiral Molecules. *Nano Lett.* **2021**, *21*, 3026−3032.

(42) Sang, Y.; Mishra, S.; Tassinari, F.; Karuppannan, S. K.; Carmieli, R.; Teo, R. D.; Migliore, A.; Beratan, D. N.; Gray, H. B.; Pecht, I.; et al. Temperature Dependence of Charge and Spin Transfer in Azurin. *J. Phys. Chem. C* **2021**, *125*, 9875−9883.

(43) Applequist, J. On the polarizability theory of optical rotation. *J. Chem. Phys.* **1973**, *58*, 4251−4259.

(44) Hache, F.; Dartigalongue, T. Application of the polarizability theory to the calculation of anisotropic circular dichroism spectra. *Chem. Phys.* **2004**, *303*, 197−203.

(45) Zhang, L.; Niu, Q. Angular Momentum of Phonons and the Einstein−de Haas Effect. *Phys. Rev. Lett.* **2014**, *112*, 085503.

(46) Juraschek, D. M.; Spaldin, N. A. Orbital magnetic moments of phonons. *Phys. Rev. Mater.* **2019**, *3*, 064405.

(47) Korenev, V. L.; Salewski, M.; Akimov, I. A.; Sapega, V. F.; Langer, L.; Kalitukha, I. V.; Debus, J.; Dzhioev, R. I.; Yakovlev, D. R.; Müller, D.; et al. Long-range p-d exchange interaction in a ferromagnet-semiconductor hybrid structure. *Nat. Phys.* **2016**, *12*, 85−91.

(48) Chen, H.; Zhang, W.; Niu, Q.; Zhang, L. Chiral phonons in two-dimensional materials. *2D Mater* **2018**, *6*, 012002.

(49) Naaman, R.; Paltiel, Y.; Waldeck, D. H. Chiral Molecules and the Spin Selectivity Effect. *J. Phys. Chem. Lett.* **2020**, *11*, 3660−3666.